Monthly Notices of the ROYAL ASTRONOMICAL SOCIETY

MNRAS **524,** 4196–4211 (2023)
Advance Access publication 2023 June 19

https://doi.org/10.1093/mnras/stad1971

Unresolved Rossby and gravity modes in 214 A and F stars showing rotational modulation

Andreea I. Henriksen,[1★] Victoria Antoci,[1★] Hideyuki Saio,[2] Frank Grundahl,[3] Hans Kjeldsen,[3] Timothy Van Reeth,[4] Dominic M. Bowman,[4] Péter I. Pápics,[4] Peter De Cat,[5] Joachim Krüger,[6,7] M. Fredslund Andersen[3] and P. L. Pallé[8,9]

[1]*National Space Institute, Technical University of Denmark, Elektrovej, DK-2800 Kgs. Lyngby, Denmark*
[2]*Astronomical Institute, Graduate School of Science, Tohoku University, Sendai 980-8578, Japan*
[3]*Stellar Astrophysics Centre, Department of Physics and Astronomy, Aarhus University, DK-8000 Aarhus C, Denmark*
[4]*Institute of Astronomy, KU Leuven, Celestijnenlaan 200D, B-3001 Leuven, Belgium*
[5]*Royal Observatory of Belgium, Ringlaan 3, B-1180 Brussels, Belgium*
[6]*Centre for Astrophysics, University of Southern Queensland, Toowoomba, QLD 4350, Australia*
[7]*Astronomical Observatory Institute, Faculty of Physics, A. Mickiewicz University, ul. Słoneczna 36, PL-60-286 Poznan, Poland*
[8]*Instituto de Astrofísica de Canarias, E-38205 La Laguna, Tenerife, Spain*
[9]*Departamento de Astrofísica, Universidad de La Laguna (ULL), E-38206 La Laguna, Tenerife, Spain*

Accepted 2023 June 21. Received 2023 June 19; in original form 2023 April 21

ABSTRACT

Here, we report an ensemble study of 214 A- and F-type stars observed by *Kepler*, exhibiting the so-called *hump and spike* periodic signal, explained by Rossby modes (r modes) – the *hump* – and magnetic stellar spots or overstable convective (OsC) modes – the *spike*, respectively. We determine the power confined in the non-resolved hump features and find additional gravity-mode (g-mode) humps always occurring at higher frequencies than the spike. Furthermore, we derive projected rotational velocities from FIES, SONG, and HERMES spectra for 28 stars and the stellar inclination angle for 89 stars. We find a strong correlation between the spike amplitude and the power in the r and g modes, which suggests that both types of oscillations are mechanically excited by either stellar spots or OsC modes. Our analysis suggests that stars with a higher power in $m = 1$ r-mode humps are more likely to also exhibit humps at higher azimuthal orders ($m = 2$, 3, or 4). Interestingly, all stars that show g-mode humps are hotter and more luminous than the observed red edge of the δ Scuti instability strip, suggesting that either magnetic fields or convection in the outer layers could play an important role.

Key words: stars: early-type – stars: oscillations – stars: rotation.

1 INTRODUCTION

Rossby or r modes (Rossby 1939; Papaloizou & Pringle 1978) are retrograde toroidal motions, which in rotating stars couple with spheroidal motions (restored by the Coriolis force) and cause temperature perturbations, generating observable effects (Saio et al. 2018a). Out of these, the toroidal component is responsible for most of the matter flow patterns on the stellar surface, while the spheroidal component causes smaller displacements.

r modes have been the subject of various other astrophysical theoretical studies (e.g. Provost, Berthomieu & Rocca 1981; Saio 1982; Andersson 1998), but it was not until photometric space missions, such as *Kepler* (Koch et al. 2010) or the Transiting Exoplanet Survey Satellite (TESS; Ricker et al. 2015), that r modes could be detected in stars. Initially reported in a sample of γ Doradus stars (Van Reeth, Tkachenko & Aerts 2016), it was later suggested that r modes could be present in other types of stars (Saio 2018; Saio et al. 2018a). From hot subdwarfs (Jeffery 2020) to intermediate-mass stars (e.g. Van Reeth et al. 2016; Saio et al. 2018a; Li et al. 2019), it appears that the latest advancement in the observational effort has revealed that r modes are seemingly common in early-type stars across their evolution.

Löptien et al. (2018) have shown the presence and importance of r modes in the shallow near-surface layers of our Sun, arguing that, as the vorticity of these waves is comparable to that of the convection, they play an essential role in solar dynamics.

Studying the signal from r modes can also prove useful in exoplanet and stellar activity studies. Lanza et al. (2019) investigated the radial velocity (RV) variation that sectoral r modes would induce in the case of solar-like stars and concluded that their signal could lead to inaccurate results if not taken into account. In addition, r modes can prove useful in studying binary systems as Saio et al. (2018a) reported the possibility of r modes to be generated by tidal disturbances in so-called heartbeat stars. A later study on 20 such tidally interacting stars (Saio & Kurtz 2022) showed that by fitting the expected visibility distribution of r modes, the stellar rotation rates could be determined.

In the case of intermediate-mass stars, analysing r modes together with gravity (g) modes helps to better understand and determine the

★ E-mail: andreea@space.dtu.dk (AIH); antoci@space.dtu.dk (VA)

© 2023 The Author(s)
Published by Oxford University Press on behalf of Royal Astronomical Society

Downloaded from https://academic.oup.com/mnras/article/524/3/4196/7210543 by University of Southern Queensland user on 14 December 2023

internal stellar rotation rate (Li et al. 2019; Takata et al. 2020). Furthermore, Saio et al. (2018a) argued that r modes could be mechanically excited by the disruption of the rotational flow on the stellar surface caused by stellar spots. This phenomenon would give rise to a specific periodic signal, *hump and spike*, found in hundreds of early-type stars (e.g. Balona 2013; Balona et al. 2015; Trust et al. 2020; Henriksen et al. 2023), where the *hump* represents unresolved r modes and the spike represents the spots that are co-rotating with the stellar surface.

Henriksen et al. (2023) showed that the spike, if due to stellar spots, could be translated into an estimate of the strength of the magnetic field, as the spike amplitudes are anticorrelated with the stellar mass, which agrees with the theoretical predictions from Cantiello & Braithwaite (2019). Furthermore, it appears that the lifetimes of the spikes are short, as expected from magnetic features of subsurface dynamo-generated fields. On the other hand, the rotational modulation that is translated into the spike could also be attributed to overstable convective (OsC) modes that resonantly excite low-frequency g modes in the stellar envelope (Lee & Saio 2020; Lee 2021). While the harmonic signatures of around 20 per cent of the *hump and spike* stars studied in Henriksen et al. (2023) indicate a signal consistent with stellar spots, for the larger part of the stars in the sample, the OsC modes cannot be ruled as the cause of *spike* feature. This calls for additional analysis to understand the phenomenon behind the *spike* feature, for example, direct magnetic field measurements.

Another approach is to study the *hump* feature since the r modes that are causing it are suggested to be connected to the phenomenon that gives rise to the *spike*. In contrast to the r modes identified in previous studies of intermediate-mass stars (e.g. Van Reeth et al. 2016; Li et al. 2019; Takata et al. 2020), the r modes hypothesized to be present in *hump and spike* stars have very high radial orders. This means that, despite the 4-yr *Kepler* data set, these modes are unresolved and a period spacing cannot be determined (Saio et al. 2018a). Here, we focus on finding correlations between the characteristics of the *hump* and the *spike*. The sample, data and analysis methods are described in Section 2. We devote Section 3 for discussing and interpreting our results. We conclude our work in Section 4.

2 DATA ANALYSIS

2.1 Sample selection

In Henriksen et al. (2023), 162 stars that exhibit the *hump and spike* feature in their Fourier spectra computed with *Kepler* data were studied. In addition to these stars, we include 52 previously discarded stars in our sample. Henriksen et al. (2023) did not analyse these targets as they showed possible signs of binarity, which would alter stellar parameters, such as $T_{\rm eff}$ or luminosity. Fig. 1 depicts some examples of such stars. We chose to include these stars in our sample, as we will search for correlation between parameters of the *hump and spike* feature, which are determined independently of stellar parameters. As mentioned in Henriksen et al. (2023), the targets were selected from literature, from works such as Balona (2013, 2014, 2017), Balona et al. (2015), Trust et al. (2020), and Santos et al. (2021) or by visually inspecting the Fourier spectra of *Kepler* time series. In total, we focus on studying 214 *hump and spike* stars by analysing photometric and spectroscopic data to shed light on the phenomenon that could cause the *hump* feature.

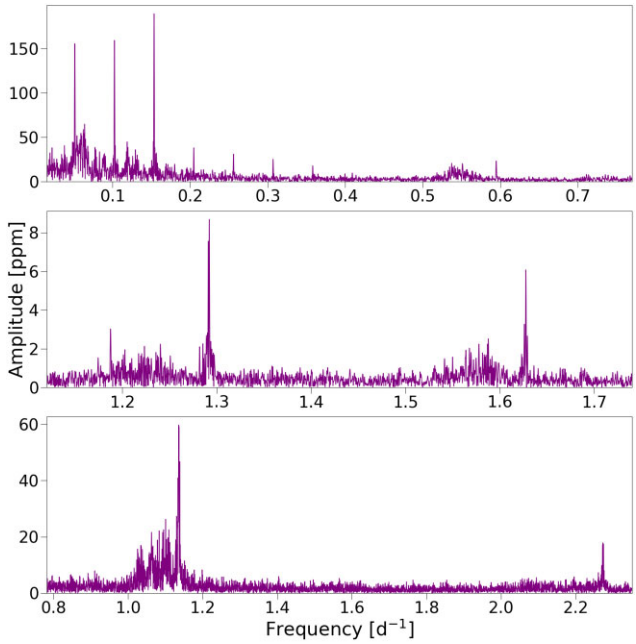

Figure 1. Fourier spectra of two targets from our sample that show signs of being in a binary system and of Tabby's star. *Upper panel*: Fourier spectrum of KIC 6116612. The *hump and spike* feature is located between ∼0.5 and 0.6 d^{-1}, while at lower frequencies (≤0.4 d^{-1}), clear periodic signal of a transiting companion. *Middle panel*: Fourier spectrum of KIC 5980337. The *hump and spike* feature appears twice in the spectrum. Given that the frequency of the second spike is not a harmonic of the first spike, it could indicate that the Fourier spectrum is a composite spectrum of two *hump and spike* stars (possibly in a binary system). *Lower panel*: Fourier spectrum of KIC 8462852 (Tabby's star) reveals a hump between ∼1.01 and 1.12 d^{-1} and a spike at ∼1.136 d^{-1}, as well as the second harmonic of the spike at ∼2.27 d^{-1}. The third harmonic is detected as well (f = 3.409 d^{-1}).

2.2 Photometry

2.2.1 *Kepler light curves*

As in Henriksen et al. (2023), we have made use of the *Kepler* long-cadence data (Koch et al. 2010), which were retrieved from Kepler Asteroseismic Science Operations Center (KASOC).[1] The Pre-search Data Conditioning data products were used in our analysis as they did not contain specific systematic errors and the *hump* signal was unaltered by the Kepler Science Operations Center pipeline (Twicken et al. 2010). Based on the quarterly stitched data, a Fourier spectrum was computed for each star, with the help of the lightcurve python package (Lightkurve Collaboration 2018). KIC 8462852 (Tabby's star; Boyajian et al. 2016) was included in our sample, and due to its challenging light curve (see Fig. 2), and rather than correcting the irregularly deep dips found in the time series, we chose to exclude parts of it. The timestamps (in BRJD – Barycentric Reduced Julian Date = BJD-2400000.0) of the excluded data, indicated with red vertical lines in Fig. 2, are as follows: between 54964 and 54976, between 55089 and 55096, between 55565 and 55640, and everything after 56305. The data in these time intervals correspond to the most significant dips in the light curve (dips 1, 2, 5, and 7–10 from Boyajian et al. 2016). For the scope of our work, we deemed that excluding the data between these time ranges was

[1] kasoc.phys.au.dk

Downloaded from https://academic.oup.com/mnras/article/524/3/4196/7210543 by University of Southern Queensland user on 14 December 2023

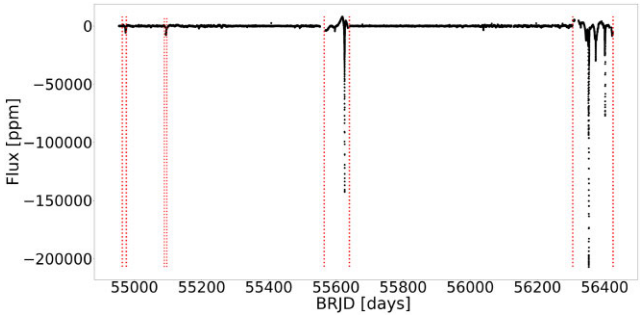

Figure 2. Light curve of KIC 8462852 (Tabby's star). The vertical red lines indicate the data that were excluded while computing the Fourier spectrum from lower panel of Fig. 1.

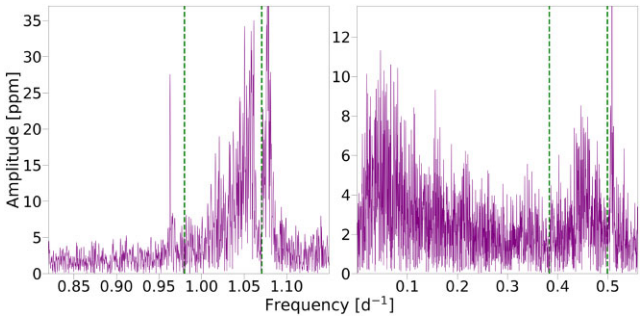

Figure 3. Two targets from our sample for which a manual selection of the hump frequency region was necessary. For a better visualization of the humps, both panels are focused on lower SNR signals than the spike, which causes the spikes to be clipped. Vertical green lines indicated the selected frequency limits. *Left-hand panel*: KIC 5632439. Spike: frequency = 1.078 d^{-1}; amplitude = 49 ppm. *Right-hand panel*: KIC 10548172. Spike: frequency = 0.508 d^{-1}; amplitude = 30 ppm.

sufficient, as this revealed the *hump and spike* signal in the Fourier spectrum (identified first by Boyajian et al. 2016) and allowed further analysis. For more information regarding the analysis of photometric data for the remaining 213 stars in our sample, the reader is referred to Henriksen et al. (J2023).

2.2.2 *Characterizing the hump*

The hump is always a broad feature proximate to a sharp *spike*, found at the high-frequency end of the hump. However, the *hump* feature differs from star to star in terms of amplitude and width. For example, in some stars, the amplitude of the highest peaks is comparable to that of the spike (upper panel of Fig. 1, left-hand panel of Fig. 3) or even higher (see more examples in fig. 1 in Henriksen et al. 2023). In other cases, the hump is significantly lower in amplitude than the spike (lower panel of Fig. 1, right-hand panel of Fig. 3; additional examples can be found in fig. 1 in Henriksen et al. 2023). Many stars exhibit spike harmonics: 194 stars (90 per cent) with second harmonic, 115 stars (53 per cent) with third harmonic, and 69 stars (32 per cent) with fourth harmonic. Occasionally, we observed also humps located before 2, 3, or 4 times the main spike frequency [116 stars with a hump before the second spike harmonic (54 per cent), 14 stars with a hump before the third spike harmonic (6 per cent), and 4 stars with a hump before the fourth spike harmonic (2 per cent)]. The hump before the main spike corresponds to $m = 1$ even r modes, while the humps located before the harmonics are $m = 2$, $m = 3$, and $m = 4$ r modes, respectively. Another feature of interest in this work, identified in 84 stars (39 per cent), is a similar, broad, unresolved hump visible at slightly higher frequencies than the main spike (see examples in Fig. 4). Saio et al. (2018a) suggested that this low-amplitude feature is a group of prograde dipole g modes. In order to make a distinction between the two types of humps, we refer to the hump located at lower frequencies with respect to the spike as r-mode hump and the one at higher frequencies as g-mode hump.

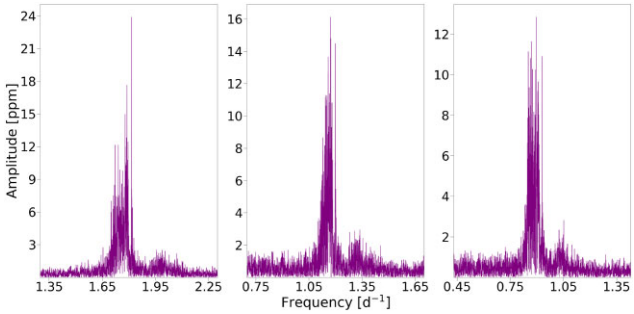

Figure 4. Example of three targets exhibiting the *hump after spike* (g-mode hump) feature. *Left-hand panel*: KIC 5524045. *Middle panel*: KIC 7842339. *Right-hand panel*: KIC 9273647.

The hump signal was identified in each Fourier spectrum and the frequency range where a hump lies was selected manually for each star. The reason why a manual selection was preferred was due to the large diversity in the hump variability from target to target, and the occasional presence of nearby peaks that should not be considered part of the hump, making automatic selection unfeasible. Two such examples are given in Fig. 3. In the left-hand panel, at around 0.95 d^{-1}, KIC 5632439 exhibits a high-amplitude peak that is unlikely to be due to an r mode given the theoretical predicted visibilities (Saio et al. 2018a). The proximity to the hump would have caused issues in the case of an automatic selection. However, we cannot exclude that the peak is an r mode excited by a different mechanism. In the right-hand panel of Fig. 3, the r-mode hump of KIC 10548172 is located close to low-frequency peaks that are likely instrumental or due to the presence of a companion. Regardless of the origin of this signal, the proximity of the hump to these peaks, in the case of an automatic selection of the hump limits, would have caused a wider frequency range selection of the hump.

The accuracy with which we have selected the hump has been tested on synthetic data. For this, we have used the frequencies and visibility of $m = 1$ even r-mode models (with rotation frequencies of $f_{\rm rot} = 1$ d^{-1} and $f_{\rm rot} = 2$ d^{-1}, inclination = 90° for both models), described and depicted in fig. 4 in Saio et al. (2018a). A synthetic time series was computed and Gaussian noise was added. Different signal-to-noise ratios (SNRs) were used, which are computed as the ratio between the highest peak and the noise level. As seen in Table 1, as the noise level increases, the low-frequency limit of the hump is less accurate. However, even in the case of no added noise, the low-frequency part of the hump cannot be recovered because of the low amplitudes of the low-frequency r modes. The high-frequency limit of the hump is recovered with more confidence because of the higher expected visibility of r modes at higher frequencies. Additionally, an observed hump is also delimited by the spike, which aids in the selection, as the frequencies of r modes ($m = 1$) are always lower than the rotation frequency ($f_{\rm rm} < f_{\rm rot}$) in the inertial frame (Saio et al. 2018a).

Downloaded from https://academic.oup.com/mnras/article/524/3/4196/7210543 by University of Southern Queensland user on 14 December 2023

Table 1. Selection of frequency limits of two theoretical r-mode humps from models with rotation frequencies of 1.0 and 2.0 d^{-1}, respectively. f_{left} and f_{right} represent the frequency limits of the humps at lower and higher frequencies, respectively. Input values are theoretical values from the model depicted in fig. 4 in Saio et al. (2018a). The selected values are average values obtained from 10 realizations. The accuracy of the selection is written in the parenthesis following each value.

Noise level	f_{left} (d^{-1}) Input	Selected	f_{right} (d^{-1}) Input	Selected
		$f_{rot} = 1.0\ d^{-1}$		
No noise	0.667	0.769 (0.001)	0.975	0.965 (0.001)
SNR ∼ 25		0.782 (0.011)		0.967 (0.003)
SNR ∼ 12		0.800 (0.011)		0.965 (0.003)
SNR ∼ 6		0.828 (0.018)		0.966 (0.009)
		$f_{rot} = 2.0\ d^{-1}$		
No noise	1.336	1.657 (0.001)	1.975	1.972 (0.004)
SNR ∼ 25		1.696 (0.016)		1.968 (0.005)
SNR ∼ 12		1.722 (0.039)		1.967 (0.006)
SNR ∼ 6		1.783 (0.024)		1.963 (0.009)

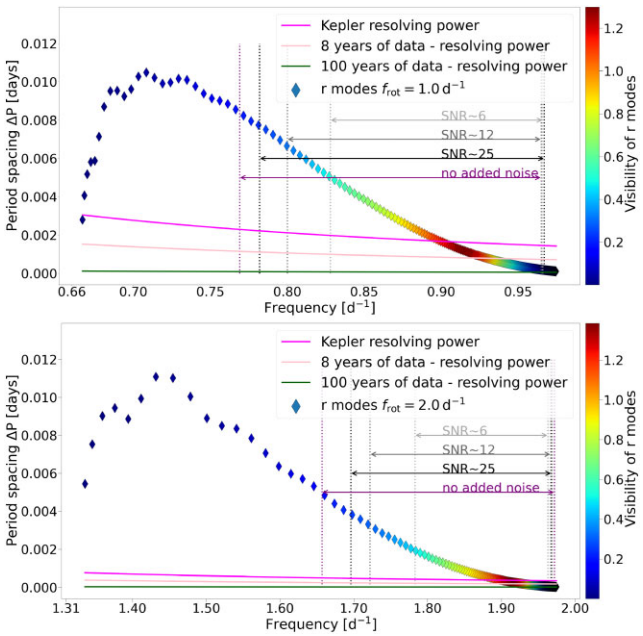

Figure 5. Period spacings of theoretical r modes based on models from Saio et al. (2018a) (see text for more details), $(m, k) = (1, -2)$ in a 1.6-$M_\odot$, T_{eff} = 7150-K, 1.89-$R_\odot$ model. The hump widths as described in Table 1 in the case of no added noise and a hump with SNR = 25, 12, and 6, respectively, are delimited by the horizontal double-sided arrows labelled accordingly. The *Kepler* resolving power is highlighted in magenta, while the resolving powers in the case of longer time series are coloured in pink (8 yr of data) and green (100 yr of data). *Upper panel*: $f_{rot} = 1.0\ d^{-1}$. *Lower panel*: $f_{rot} = 2.0\ d^{-1}$.

2.2.3 *r-mode detectability*

The r modes identified in previous studies of intermediate-mass stars (Van Reeth et al. 2016; Li et al. 2019; Takata et al. 2020) were resolved, and so a period spacing could be determined. In our case, however, as Saio et al. (2018a) pointed out, r modes cannot be resolved despite the 4-yr *Kepler* data set. This is because of their very high radial orders and small period spacings, as illustrated in Fig. 5, where we depict the same two synthetic models mentioned in Section 2.2.2. While the period spacing at low frequencies is large enough

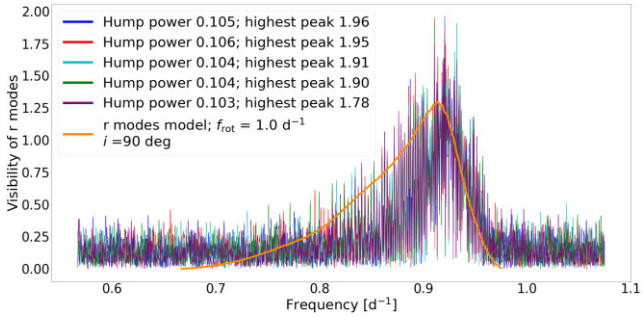

Figure 6. Five realizations of synthetic humps with the same noise level (approx. SNR = 11). The power and highest peak for each realization are displayed in the legend. Due to noise, the highest peak is not a representative measure for the size of the hump.

to be detected with the *Kepler* resolving power, the visibility of the r modes at lower frequencies is too low for them to be identified (see the colour bar in Fig. 5). In Fig. 5, the vertical lines, annotated with the double-sided arrows, delimit the selected frequency interval from Table 1. Furthermore, despite the r-mode peaks being visible at higher frequencies, the period spacing becomes too small to be detectable with the *Kepler* data set. Not even with a time series twice as long would all the r modes in the hump be resolved. For the two cases displayed here, a time series of 100 yr would be necessary in order to resolve all the r modes. This indicates that the widths of the selected humps in this work are underestimated at the lower frequency limit and that, in fact, r modes span over wider frequency ranges. The selected width of the theoretical r-mode humps spans from 0.15 to 0.3 d^{-1} (depending on the rotation frequency or noise level, see Table 1 and Fig. 5). This is in agreement with the selected widths of the observed humps of our stars. The average hump width in our sample is ∼0.1 d^{-1}, while the maximum and minimum hump widths are ∼0.21 and ∼0.022 d^{-1}, respectively. For around 70 per cent of our stars, the SNR of the r-mode hump is lower than 30.

2.2.4 *The power of the humps*

In order to quantify the *hump* features (whether r or g modes), we calculated the power of the humps. We chose to do so because the hump is unresolved and the highest peak is not a representative measure for the hump, as the amplitude of a peak may change due to noise. We illustrate this aspect in Fig. 6, where for the same noise level but different realizations, the highest peak in the hump varies significantly, while the variation in power only slightly. To simulate these data, we use the same model ($f_{rot} = 1.0\ d^{-1}$) as in Section 2.2.3.

The power under the hump was calculated using the integrate.simpson function from SCIPY PYTHON package (Virtanen et al. 2020), which implements the composite Simpson's rule. This was done directly on the Fourier spectrum. We have accounted for the fact that the noise level in the Fourier spectrum differs from star to star by computing the noise in each observed spectrum and then subtracting its power from the power contained by the hump. The noise level was estimated in a frequency range between ≈15 and ≈24 d^{-1}. The Fourier spectrum of each target was inspected independently to ensure that no astrophysical signal was included in the noise determination. We then computed artificial light curves that contained only the noise levels using the *Kepler* timestamps of each star and determined the power (amplitude squared – ppm^2) contained in the frequency range defined by the humps. Furthermore,

Downloaded from https://academic.oup.com/mnras/article/524/3/4196/7210543 by University of Southern Queensland user on 14 December 2023

to account for the shorter time series in some cases, we have divided the calculated hump power by the power of the spectral window, which we calculated with equation (1):

$$\mathrm{Pw_{SW}} = \frac{1}{N\,\Delta\,T}, \tag{1}$$

where N is equal to the total number of data points in the time series and $\Delta\,T$ is the median value of the cadence of the time series. The resulting unit of the power under the hump is therefore ppm^2 d.

2.3 Spectroscopic data

We have analysed spectroscopic data for 28 *hump and spike* stars. Most spectroscopic data were acquired with the optical échelle spectrograph FIES, located at the 2.56-m Nordic Optical Telescope in La Palma, Spain. The FIES spectra were obtained through dedicated proposals during the observing periods 64 and 65, using the high-resolution fibre (#4), which offers a spectral resolution of $R \sim 67\,000$ (Telting et al. 2014). The data products used in our analysis were the output of the automated data reduction pipeline – FIEStools (v. 1.5.2)[2].

Additional spectra were acquired for a few stars from our sample with the Hertzsprung SONG Telescope (a node of the Stellar Observations Network Group) located at Observatorio del Teide (Fredslund Andersen et al. 2019). The spectra were obtained with the 1.2-arcsec slit, corresponding to a resolution of $R \sim 90\,000$.

We have also made use of archival data obtained with the high-resolution spectrograph HERMES ($R \sim 85\,000$) at the Mercator telescope (Raskin et al. 2011). The metadata (filename, instrument, date of acquisition, and exposure time) of the spectra analysed in the current work can be consulted in Table A1.

The spectroscopic data served two purposes: (i) to detect any RV shift that might indicate the presence of a stellar companion; and (ii) to measure the projected rotational velocity, which combined with the rotational period obtained from photometric data from the spike frequency, would help in estimating the stellar inclination.

In addition to the spectroscopic data analysed in this work, we have also gathered $v \sin i$ values reported in literature for 61 targets from our sample. The sources of the $v \sin i$ values are given in Table A2.

In the following sections, we describe in more depth the spectroscopic analysis methods used to achieve these goals.

2.3.1 Synthetic spectra

Synthetic spectra were used as templates in determining radial velocities and aided in the spectral line selection, when estimating the projected rotational velocities ($v \sin i$). The spectra were computed with the stellar spectral synthesis program SPECTRUM v2.77c (Gray & Corbally 1994).[3]Synthetic spectra were computed with ATLAS9 stellar atmosphere models [4] (Castelli & Kurucz 2003).

For choosing an appropriate stellar atmosphere model that would be representative for each star, the $T_{\rm eff}$ and $\log g$ values were used. $T_{\rm eff}$ values were taken from *Gaia* Data Release 2 (DR2; Gaia Collaboration 2018) and can be found in Table A3. The $\log g$ values can be found in Table 4, where the source is indicated in the footnote.

The synthetic spectra were computed in the wavelength range from 4000 to 6800 Å. The obtained spectra were also rotationally broadened with the AVSINI function in SPECTRUM with 30, 65, 100, and 150 km s^{-1}. These values were chosen as the average $v_{\rm rot}$ value for *hump and spike* stars is ~150 km s^{-1} (see Table A3 and fig. 8 in Henriksen et al. 2023), while 100, 65, and 30 km s^{-1} are representative values for the slower rotating star. The limb-darkening coefficient used was 0.6 for all spectra (linear limb-darkening law; see equation 17.11 in Gray 2005). This value is a good approximation given the $T_{\rm eff}$ range in which our stars lie (see e.g. Gray 2005, p. 437). In the following section, we describe the observed spectroscopic data analysis.

2.3.2 Radial velocity

For stars with spectra observed on at least two different nights, RV shifts were determined. The RV shifts between the two epochs were extracted by cross-correlating the observed with corresponding synthetic spectra, using the function *cross_correlate_with_template*, from the ISPEC software solution (Blanco-Cuaresma et al. 2014; Blanco-Cuaresma 2019). For the FIES and SONG spectra, the cross-correlation was performed for each échelle order. The final RV value and its uncertainty were calculated as a weighted average of the individual RVs from each échelle order and as the error on the weighted mean, respectively, using equations (2) and (3). The RV uncertainties for each échelle order ($\sigma_{\rm RV_{order}}$) are calculated through ISPEC, which implements the maximum-likelihood approach given by Zucker (2003). The fitting model used in this work was a second-order polynomial and a Gaussian. The reader is referred to the ISPEC documentation for more details (Blanco-Cuaresma et al. 2014; Blanco-Cuaresma 2019).

$$\mathrm{RV_{final}} = \frac{\sum \mathrm{RV_{order}}/\sigma^{-2}_{\mathrm{RV_{order}}}}{\sum \sigma^{-2}_{\mathrm{RV_{order}}}}. \tag{2}$$

$$\sigma_{\mathrm{RV_{final}}} = \frac{1}{\sum \sigma^{-2}_{\mathrm{RV_{order}}}}. \tag{3}$$

Orders that contained telluric lines or broad lines (such as Hα or Hβ), or which did not contain any spectral lines, were excluded. The telluric lines atlas that was used for guidance is the telluric mask that ISPEC provides (Blanco-Cuaresma et al. 2014) and which is based on synthetic spectrum described in more detail in Bertaux et al. (2014).

In the case of HERMES spectra, we worked with order-merged, 1D wavelength-calibrated spectra. For computation purposes, and in order to avoid regions where telluric lines were present, the spectra were clipped into 13 sections (Table A4 contains the wavelength limits of these sections). The final RV values were computed as the weighted average from those obtained from each of the 13 sections. The results of our analysis can be seen in Table 2, for stars with two or more available epochs, and in Table 3, where only one epoch was observed. We consider epochs separate when the data originate from different observing nights. The instrument used is specified in the aforementioned tables. The results in Table 2 indicate that out of the 22 stars for which an RV shift could be determined, 11 stars show signs for possible stellar companions. We classified a star as binary when the RV measurements from the different epochs were discrepant based on the 3σ uncertainties. We note that the stars indicated as non-binary could still have a companion that eluded our observations.

This means that 11 stars out of 22 *hump and spike* stars for which we could gather RV information could be part of binary (multiple) systems. Depending on the literature source, the binary occurrence

[2]www.not.iac.es/instruments/fies/fiestool/FIEStool.html
[3]www.appstate.edu/~grayro/spectrum/spectrum.html
[4]https://wwwuser.oats.inaf.it/castelli/grids/gridp05k2odfnew/ap05k2tab.html

Downloaded from https://academic.oup.com/mnras/article/524/3/4196/7210543 by University of Southern Queensland user on 14 December 2023

Table 2. Overview of RV results for stars with multiple epochs. The instrument with which the data were obtained is indicated in parenthesis under the KIC ID. Table A1 contains the list of all available spectra.

KIC (Instrument)	Mid-point of obs. [Y-M-D h:m] UT	RV ($km\,s^{-1}$)	$3\sigma_{RV}$ ($km\,s^{-1}$)	Binary?
3634487	2022-06-20 00:36	6	8.6	n
(FIES)	2022-05-27 00:38	13	7.2	
3848948	2022-06-20 03:55	−6	5.7	n
(FIES)	2022-05-26 02:10	0	1.6	
4572373	2012-07-14 01:55	9	7.3	n
(HERMES)	2012-09-05 00:43	4	8.4	
	2012-09-05 01:13	0	2.9	
4661914	2022-06-20 02:14	−21	1.6	y
(FIES)	2022-05-26 04:06	−10	1.4	
4856799	2022-06-20 04:53	−17	9.8	y
(FIES)	2022-05-27 05:08	−2	3.9	
5024410	2013-07-26 22:47	3	0.03	y
(HERMES)[a]	2013-07-28 01:28	4	0.03	
	2013-07-30 00:14	2	0.03	
	2013-10-01 20:55	−9	0.03	
	2013-10-04 21:42	−10	0.03	
	2021-08-21 02:11	−2	0.03	
5456027	2022-06-20 01:50	−2	2.8	n
(FIES)	2022-05-26 04:52	−0	1.5	
5524045	2011-09-19 22:37	−4	4.5	n
(HERMES)	2018-11-06 22:05	−5	3.3	
	2018-11-06 22:26	−3	3.1	
5980337	2022-06-20 02:37	10	3.0	y
(FIES)	2022-05-26 02:36	22	3.0	
6039039	2022-06-21 01:19	0	2.3	y
(FIES)	2022-05-27 03:41	11	2.5	
6610433	2022-06-06 04:35	−17	4.3	n
(FIES)	2022-06-21 00:49	−9	4.6	
7116117	2022-06-20 01:04	−21	0.8	y
(FIES)	2022-05-27 04:40	−10	0.7	
7131587	2021-10-04 21:09	30	1.1	n
(FIES)	2021-10-10 21:54	29	1.1	
7842339	2021-10-04 21:42	10	4.4	n
(FIES)	2021-10-10 22:32	17	5.3	
7939835	2022-06-21 00:22	−5	0.3	y
(FIES)	2022-05-27 00:11	7	0.3	
7959579	2022-06-20 01:26	−14	4.9	y
(FIES)	2022-05-26 04:27	−1	1.4	
8037519	2018-09-06 21:32	15	12.0	y
(SONG)	2021-06-16 01:20	−11	9.6	
(HERMES)	2016-04-12 05:08	30	19.8	
	2016-04-13 03:37	29	18.7	
9117875	2011-07-11 22:30	0	1.0	n
(HERMES)	2011-07-12 22:33	0	0.9	
9273647	2022-06-20 03:34	−26	2.4	y
(FIES)	2022-05-26 01:48	−15	2.4	
9519698	2022-06-19 05:15	−3	7.2	n
(FIES)	2022-05-26 03:29	1	4.6	
10068389	2022-06-19 05:01	−34	7.0	n
(FIES)	2022-05-26 03:44	−33	7.3	
10810140	2022-06-20 04:24	−11	5.0	y
(FIES)	2022-05-27 04:12	−1	2.1	

[a]More data available for this target.

in chemically normal A stars is between 35 and 60 per cent (Patience et al. 2002; Eggleton & Tokovinin 2008; Abt 2009), which is consistent with our results. However, we consider that a more extensive study regarding the binary occurrence is needed, as the number of stars is too small and additional data points are needed to establish the presence of stellar companions.

Table 3. Overview of RV results for stars with one epoch. The data are sorted by instrument. For targets with multiple observations, the listed RV and uncertainties values are average values.

KIC	Mid-point of obs. [Y-M-D h:m] UT	RV ($km\,s^{-1}$)	$3\sigma_{RV}$ ($km\,s^{-1}$)
	FIES		
4066110	2021-10-16 21:29	45	1.2
	2021-10-16 21:55		
	2021-10-16 22:20		
5566579	2021-10-03 22:40	−2	2.7
	2021-10-03 23:09		
5903499	2021-10-14 21:17	0	5.3
	2021-10-14 21:48		
5938266	2021-10-03 21:34	23	1.9
	2021-10-03 22:05		
6974705	2021-10-12 22:24	11	7.6
	2021-10-12 22:50		
8846809	2021-10-12 21:50	1	1.9
	SONG		
8783760	2021-06-21 01:26	−6	6.3
9163520	2018-09-28 23:27	−19	0.4
	2018-09-28 23:35		
	2018-09-28 23:43		
	HERMES		
6192566	2011-09-19 21:01	−29	2.4

The results presented in Table 3 were used to shift the observed spectra to align with the synthetic spectra, for an easier identification of spectral lines that could be used in computing the projected rotational velocities. This method is described in the following section.

2.3.3 $v \sin i$ *determination – the Fourier method*

To extract the projected rotational velocities ($v \sin i$) from the available spectroscopic data, the Fourier technique was adopted. As described by Smith & Gray (1976) and applied in works such as Royer et al. (2002a, b) or Simón-Díaz et al. (2006), the Fourier transform of a spectral line produces a curve with sidelobes that alternate in being either dips or peaks and will gradually flatten in amplitude. Examples of such curves are displayed in Fig. 7, where the Fourier transforms of an iron line (Fe I 6065.48 Å), found in the observed spectra of KIC 7116117 and KIC 5938266, are compared with the Fourier transforms of the corresponding synthetic spectral line found in rotationally broadened synthetic spectra. The frequency of the first zero (dip) in the Fourier transform of the line profile corresponds to the last dip in velocity space, which indicates the value of the $v \sin i$. The Fourier transform was done using the spectra.tools.vsini function from the Institute of Astronomy at KU Leuven (IVS) PYTHON package.[5] If multiple spectra were available for a target, the technique was applied on the stacked spectrum. The spectra were combined by using the weighted average flux values, if flux errors were available (FIES and SONG spectra) or only the average flux values (HERMES spectra).

We tested the Fourier technique on two stars with known $v \sin i$ values from literature with which we compared our results. KIC 9117875, a relatively slow rotator (with respect to the most stars in our sample), has a literature $v \sin i$ value of 61 ± 3 $km\,s^{-1}$ (Niemczura et al. 2015). We find an average of 57 ± 6 $km\,s^{-1}$,

[5]https://github.com/IvS-KULeuven/IvSPythonRepository

Downloaded from https://academic.oup.com/mnras/article/524/3/4196/7210543 by University of Southern Queensland user on 14 December 2023

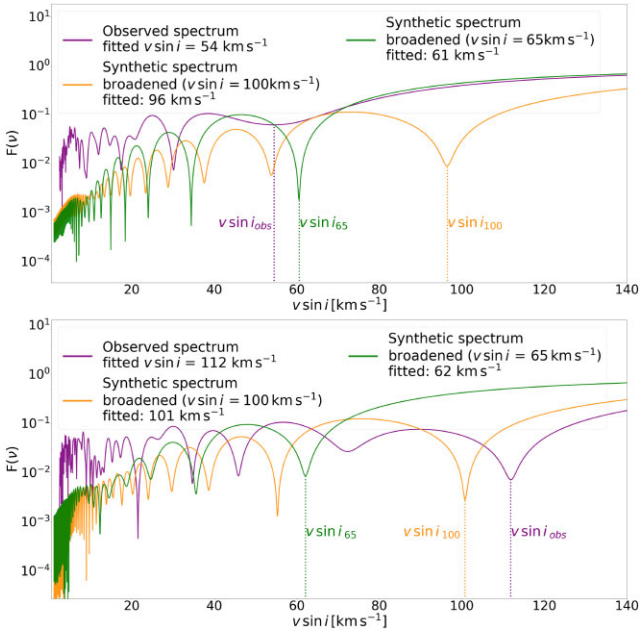

Figure 7. Fourier transform of the rotation profile for the spectral line Fe I 6065.48 Å. *Upper panel*: KIC 7116117 – Fourier transform for the observed spectral line and the spectral line of two synthetic spectra that were rotationally broadened with 65 and 100 km s^{-1}. *Lower panel*: KIC 5938266 – Fourier transform for the observed spectral line and the spectral line of two synthetic spectra that were rotationally broadened with 65 and 100 km s^{-1}. We note that both panels are similar to fig. 3 in Royer et al. (2002a); however, we prefer to display the inverse of the frequency obtained through the Fourier transform, as it is equivalent to the $v \sin i$ value.

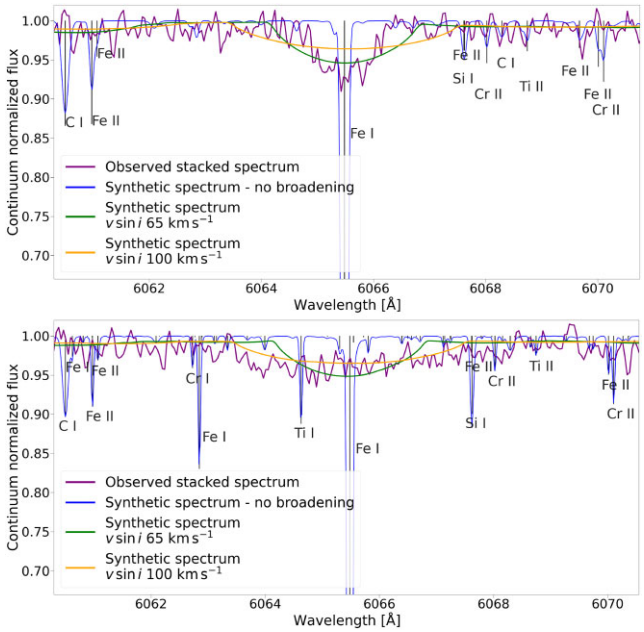

Figure 8. Observed and synthetic spectral line – Fe I 6065.48 Å. Synthetic lines rotationally broadened by 65 and 100 km s^{-1} are also displayed for comparison. For clarity, only strong lines are labelled. Both spectra are taken with FIES. *Upper panel*: KIC 7116117. *Lower panel*: KIC 5938266. One can see the appearance of more species as this target is ∼1200-K cooler than the one in the upper panel.

based on four lines: Fe I 5633.98 Å (65.5 km s^{-1}), Fe I 6065.48 Å (54.2 km s^{-1}), Fe I 6078.49 Å (58.1 km s^{-1}), and Fe I 6393.61 Å (50.5 km s^{-1}). The second test star to validate the method is KIC 4572373, a fast rotator, and has been reported to have a projected rotational velocity value of 184 ± 7 kms^{-1} (Niemczura et al. 2015). Given its $T_{\rm eff}$ and fast rotation, there were not many lines to choose from. We used Mn II 4481.13/33 (173 km s^{-1}) and Si II 6371.35 (215 km s^{-1}) to derive an average $v \sin i$ value of 194 ± 21 km s^{-1}, which is in agreement with the value reported in literature. This indicates that our method of measuring $v \sin i$ from spectral lines yields reliable results.

The selection of the wavelength range that would define a spectral line was done manually for each star and line. This was due to the fact that the wavelength range that described a spectral line depended on the rotational broadening of the star. In Fig. 8, the Fe I 6065.48-Å spectra line is displayed for two of our analysed targets: KIC 7116117 and KIC 5938266. A synthetic spectrum is also depicted together with the observed data. The synthetic spectrum was rotationally broadened with indicated values as described in Section 2.3.1. The species displayed were obtained with the LINES function from the SPECTRUM software solution. The atomic data file used in compiling a line list was the standard atomic and molecular data file, provided by SPECTRUM and which is based on Grevesse & Sauval (1998). The vertical grey lines show the contribution of the species indicated by the annotated texts. The location and the nature of the spectral lines are useful when choosing adequate spectral lines for determining the rotational broadening (lines that are fairly strong and as 'isolated' (less contaminated) as possible are preferred). This, however, is not always possible, as in some cases the high rotation makes it impossible to find 'ideal' lines, as they are either not very strong or contaminated. This task has proved to be difficult for both hot stars, where less species can be found in comparison with cooler counterparts, and for cool stars, where presence of more spectral lines implies higher chance of blending (e.g. see the difference in the same wavelength region of the observed spectrum of KIC 7116117 and KIC 5938266 in Fig. 8).

The results of our $v \sin i$ analysis using the Fourier technique can be found in Table 4, where the average $v \sin i$ values and the number of lines used are listed for each star. In Appendix A, the $v \sin i$ computed from each line can be found (Table A5). Note that uncertainties reported in Table 4 are the standard deviations of the mean values. For this reason, the uncertainties are underestimated for some targets for which $v \sin i$ measurements are accurate.

For KIC 5903499 and KIC 6974705, we note that the line selection was restricted by the high rotation rate and $T_{\rm eff}$ of the stars (see Table A3). Using the rotational frequency from the spike and the stellar radii from Berger et al. (2020), we derive rotational velocities of 200^{+10}_{-9} and 196^{+7}_{-6} km s^{-1}, respectively. The $v \sin i$ values could be measured based on only one line (the doublet Mn 4481.13/33). Furthermore, these two targets are relatively faint (KIC 5903499 – $V = 10.7$; KIC 6974705 – $V = 10.5$). Both targets were planned to be observed with FIES in two separate epochs in our observing proposal, but one of the planned observations was lost due to bad weather. This means that the observed spectra have also low SNR and measuring the rotational broadening on spectral lines is difficult. In fact, for KIC 5903499 it was very hard to measure the RV shift with respect to the synthetic spectra, due to the lack of resolved spectral lines. Only three of the échelle orders were used.

We have a similar remark regarding KIC 8037519. The combination with high $T_{\rm eff}$ and $v_{\rm rot}$ (Table A3) made it difficult to find spectral lines. We give an estimated $v \sin i$ based on the Mn 4481.13/33-Å doublet line and the 6371.35-Å Si II line. We note that the Si line has

Downloaded from https://academic.oup.com/mnras/article/524/3/4196/7210543 by University of Southern Queensland user on 14 December 2023

Table 4. Extracted $v \sin i$ values with Fourier technique. The superscript in the $\log g$ column indicates the source of the values. The last column indicates the number of lines on which the Fourier transform was applied and contributed to obtaining the final $v \sin i$ values.

KIC	$\log g^a$ (dex)	$v \sin i$ (km s^{-1})	No. of lines
3634487	3.9 ± 0.08^{m}	175 ± 14	4
3848948	4.1 ± 0.09^{m}	98 ± 12	4
4066110	3.5 ± 0.07^{m}	138 ± 19	3
4661914	4.2 ± 0.1^{m}	85 ± 14	4
4856799	4.0 ± 0.07^{m}	173 ± 14	5
5024410	3.8 ± 0.21^{b}	7 ± 2	25
5456027	4.0 ± 0.09^{m}	160 ± 6	4
5566579	4.1 ± 0.09^{m}	141 ± 20	3
5903499	4.2 ± 0.1^{m}	254	1
5938266	3.8 ± 0.08^{m}	103 ± 16	4
5980337	3.9 ± 0.12^{f}	86 ± 17	4
6039039	3.9 ± 0.07^{m}	77 ± 6	5
6192566	3.6 ± 0.09^{m}	51 ± 11	6
6610433	4.1 ± 0.08^{m}	118 ± 6	4
6974705	4.0 ± 0.08^{m}	246	1
7116117	4.0 ± 0.1^{m}	70 ± 10	4
7131587	4.0 ± 0.09^{m}	49 ± 8	15
7842339	3.9 ± 0.09^{m}	104 ± 11	3
7939835	4.0 ± 0.09^{m}	24 ± 6	14
7959579	4.2 ± 0.1^{m}	117 ± 5	4
8037519	3.9 ± 0.05^{b}	186 ± 10	2
8783760	3.9 ± 0.09^{m}	127 ± 16	5
8846809	3.7 ± 0.09^{m}	154 ± 10	3
9163520	3.5 ± 0.29^{l}	41 ± 4	6
9273647	4.0 ± 0.1^{m}	116 ± 6	4
9519698	4.0 ± 0.08^{m}	175 ± 6	5
10068389	3.9 ± 0.08^{m}	132 ± 9	5
10810140	4.2 ± 0.07^{m}	130 ± 5	5

[a]m = Murphy et al. (2019); b = Berger et al. (2020); f = Frasca et al. (2016); and l = Luck (2014).

some contamination from other species, but given the fast rotation of this star, the blending effect is negligible. The obtained values can be consulted in Table A5.

As noted in Gray 2005, for slow rotators, other broadening factors such as micro- or macro-turbulence become significant and should be accounted for when fitting the rotational broadening of spectral lines. In other words, our results for relatively slow rotators, such as KIC 5024410 and KIC 7939835, for which we measure low projected rotational velocities, (relative with respect to the other *hump and spike* stars for which the rotational velocity spans from ∼50 to ∼ 300 km s^{-1}; see fig. 8 in Henriksen et al. 2023) might not be as accurate and should be regarded with caution. More in-depth analysis should be conducted for these targets; however, we consider these values to be sufficiently accurate for the scope of this work.

2.4 Stellar inclination estimate

We show the $v \sin i$ values (determined here and from literature) as a function of $v_{\rm rot}$ in Fig. 9. The uncertainties associated with $v_{\rm rot}$ were obtained through error propagation using the radii and $f_{\rm rot}$ uncertainties listed in Table A3. There are two stars for which the rotational velocities obtained do not agree with the measured $v \sin i$ (highlighted with magenta squares: KIC 5903499 and KIC 6974705).

There are a few reasons that can explain the discrepancy between the $v_{\rm rot}$ and $v \sin i$ values. First, the uncertainties in the stellar radii, which propagate into the $v_{\rm rot}$ determination, could be underestimated.

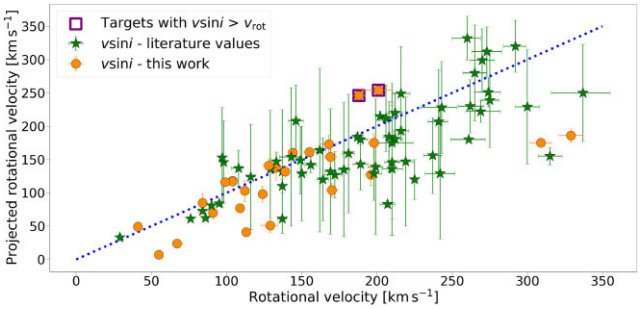

Figure 9. Projected rotational velocity values as a function of rotational velocity values. The dotted blue line stands for the one-to-one relation. Stars for which $v \sin i$ values were determined in this work are depicted with orange circles. A green star marker indicates targets for which the $v \sin i$ values are found from literature as indicated in Table A2. Targets where $v \sin i > v_{\rm rot}$ are highlighted with purple squares.

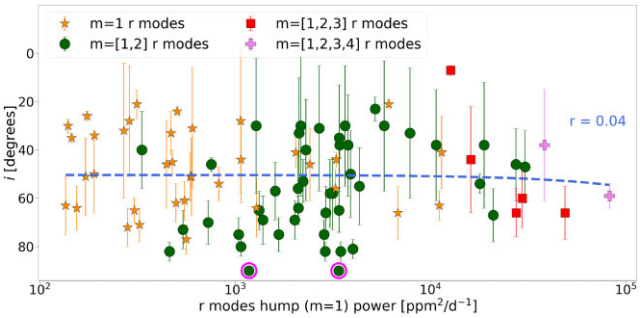

Figure 10. The power in the main hump as a function of the stellar inclination. Targets circled with magenta have the inclination set to 90°. See Section 2.4 for more details. The symbol type denotes how many r-mode humps a star possesses (e.g. the orange star symbol indicates that a target exhibits only one $m = 1$ r-mode hump, while green circles indicate that a star exhibits both $m = 1$ and $m = 2$ r-mode humps).

Secondly, since we could not rule out the presence of stellar companions (both these stars were observed with FIES in one only night, see Table 3), it is possible for their radii to be inaccurate as they could be binaries. Thirdly, as mentioned in the previous section the combination of low SNR, fast rotation, and high $T_{\rm eff}$ made it difficult to find spectral lines suitable for the Fourier method. Since we could only use the Mn doublet, we could not compute a standard deviation as an estimate for the uncertainty. As Royer et al. (2002a) noted, the $v \sin i$ error is expected to increase as the nominal value increases, because spectral lines become shallower and the occurrence of line blending increases. We choose to set the inclination values for these two stars to 90°. In Fig. 10, they are highlighted with magenta circles and are not taken into account when the correlation factor is calculated.

For the remaining stars, we have calculated the stellar inclination (i) with the equation

$$i = \arcsin\left(\frac{v \sin i}{v_{\rm rot}}\right). \quad (4)$$

Given the non-linearity of the arcsin function and its asymptotic behaviour for values close to unity, calculating the uncertainties associated with the stellar inclination cannot be done by error propagation assuming a linear combination of variables, or by approximating with a first-order Taylor series expansion. Furthermore, in the case of some stars, the $v \sin i$ values are higher than the $v_{\rm rot}$ values, which

Downloaded from https://academic.oup.com/mnras/article/524/3/4196/7210543 by University of Southern Queensland user on 14 December 2023

makes it impossible to calculate the inclination, as arcsin is not defined for values higher than unity. For this reason, we have chosen to estimate the stellar inclination and its associated uncertainty by random sampling, drawing 10^7 values for both $v \sin i$ and $v_{\rm rot}$, from truncated normal distributions centred at the nominal values and with width of the associated uncertainties ($3\,\sigma$). The reported values in Table A2 are the mean and standard deviation of the resulting distribution of calculated inclinations.

We note that despite measuring a $v \sin i$ value for KIC 5980337, we do not report an inclination value as it cannot be assessed which of the two spikes should be used in calculating the $v_{\rm rot}$ (see Fig. 1).

3 RESULTS AND DISCUSSION

In this section, we present our results based on photometric and spectroscopic observations. From photometric data, we have extracted the power of the r- and g-mode humps and we used the spike amplitudes and frequencies as derived in Henriksen et al. (2023). Combining spectroscopic and photometric data has allowed us to compute estimates of stellar inclination values. We show various correlations based on parameters described in the previous sections, as well as other stellar parameters, such as $T_{\rm eff}$ or luminosity, using similar sources as in Henriksen et al. (2023).

In Fig. 10, we depict the stellar inclination as a function of the power described by the main hump ($m = 1$ r modes). The colour code of the figure suggests that the inclination does not play a role in the visibility of the number of azimuthal orders excited in the star. The notable trend is that, with the exception of one star, all stars have an inclination $>20^\circ$. Furthermore, it seems that stars with very large power in their ($m = 1$) r-mode humps have intermediate inclination values (approx. $55^\circ \pm 10^\circ$). This is in agreement with r modes tending to be confined in mid-latitudinal regions rather than the equator (Lee & Saio 1997; Saio et al. 2018a) and therefore the visibility of r modes would be at maximum at intermediate inclinations. However, given the large uncertainties associated with the derived stellar inclination angles (Fig. 10), it is difficult to fully understand how the star's inclination influences the visibility of r modes.

The upper panel of Fig. 11 shows a moderate correlation between the $m = 1$ r-mode hump and the amplitude of the spike, suggesting that if stellar spots are responsible for the spike, then a stronger deviation of the flow, induced by magnetic fields, results in higher power r modes (a similar correlation is also found between the $m = 2$ r-mode hump and the amplitude of the spike – lower panel of Fig. 11). In the case of OsC modes, this would indicate a stronger coupling between the resonantly excited g modes by the convective core and the mechanically excited r-mode humps. In addition, the colour scheme of Fig. 11 (upper panel) shows that stars with humps at high azimuthal orders have more power in the r-mode hump at $m = 1$. This means that there is a certain lower power limit for $m = 1$ r modes required in order for $m \geq 2$ to be excited and/or visible.

In Fig. 12, the stars that possess a g-mode hump are depicted in a Hertzsprung-Russell (HR) diagram together with stars that do not. It is interesting that g-mode humps appear in stars hotter than the red edge of the observed δ Scuti instability strip from Murphy et al. (2019) (we note that the lack of stars with $T_{\rm eff} > 10\,000$ K is a selection bias, as discussed in Henriksen et al. 2023). If the spike is caused by magnetic stellar spots, this may indicate an interaction between the g modes in the cooler stars and magnetic fields, leading to possible damping. However, the correlation between g-mode humps and the spike amplitudes shown in Fig. 13 suggests a different or a more complex explanation.

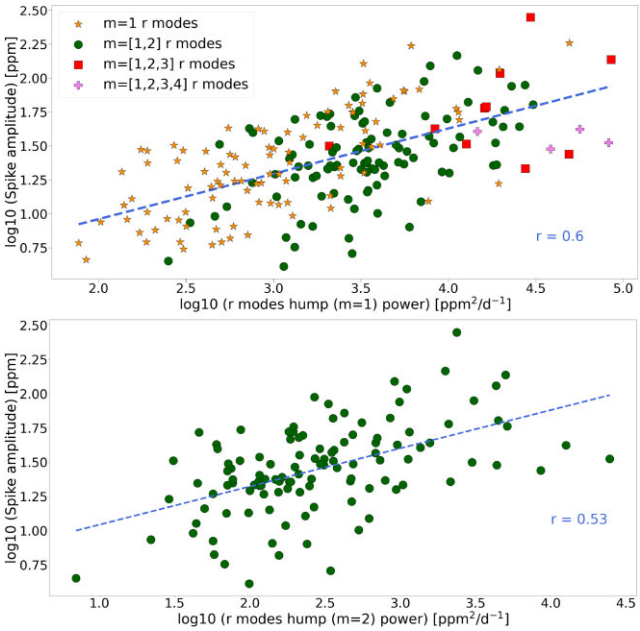

Figure 11. *Upper panel*: Moderate–strong correlation ($r = 0.6$) between power in the $m = 1$ r-mode hump and amplitude of the main spike. Both spike amplitude and power in the $m = 1$ r-mode hump can be consulted in Table A3. The colour coding is similar to that of Fig. 10, where, for example, $m = [1, 2, 3]$ r modes means that a star exhibits all $m = 1$, $m = 2$, and $m = 3$ r-mode humps. *Lower panel*: Moderate correlation ($r = 0.53$) between power in the $m = 2$ r-mode hump and amplitude of the main spike. The power in the $m = 2$ r-mode hump can be consulted in Table A6.

The relationship between the moment of inertia and oscillation frequency of g modes provides insights into the possible cause of missing g-mode humps, as well as the reason why the frequencies of g-mode humps are separated from the spike frequency by approximately 0.1 to 0.25 $\rm d^{-1}$. The moment of inertia of an oscillation mode k is defined as

$$I_k = \int_0^M \xi_k \cdot \xi_k r^2 {\rm d}M_r, \tag{5}$$

where $\boldsymbol{\xi_k}$ is the displacement vector of the mode.Fig. 14 shows the moment of inertia versus frequency of dipole prograde g modes in selected stellar models, in which I_k is normalized by $4\pi R^5 \rho_{\rm c}$ with R and $\rho_{\rm c}$ being the stellar radius and the central density, respectively. The g-mode frequencies and corresponding eigenfunctions are obtained using the traditional approximation of rotation, as described by Saio et al. (2018b). For our calculations, we have adopted a rotation frequency of $1\,{\rm d}^{-1}$ as a representative rotation (or spike) frequency (Fig. 15). We have adopted the stellar models obtained in Saio et al. (2021) where the MESA code was used (v.7184; Paxton et al. 2011, 2013, 2015) with an initial chemical composition of (X, Z) = (0.72, 0.014). The convective core boundary was determined by the Schwarzschild criterion, without including a core overshooting parameter. The elemental diffusion was activated for a smooth Brunt–Väisälä frequency. In order to avoid the settling of too much helium, the radiation turbulence was also activated. Rotational deformation was not taken into account. The oscillation energy of a mode is given as $\frac{1}{2}\sigma_k^2 I_k$ with the angular frequency of the mode σ_k. Therefore, modes with a smaller moment of inertia should be excited to larger amplitudes under some mechanical disturbances than modes with a larger moment of inertia. A g-mode hump would therefore be formed around a minimum in the I_k versus frequency relation.

Downloaded from https://academic.oup.com/mnras/article/524/3/4196/7210543 by University of Southern Queensland user on 14 December 2023

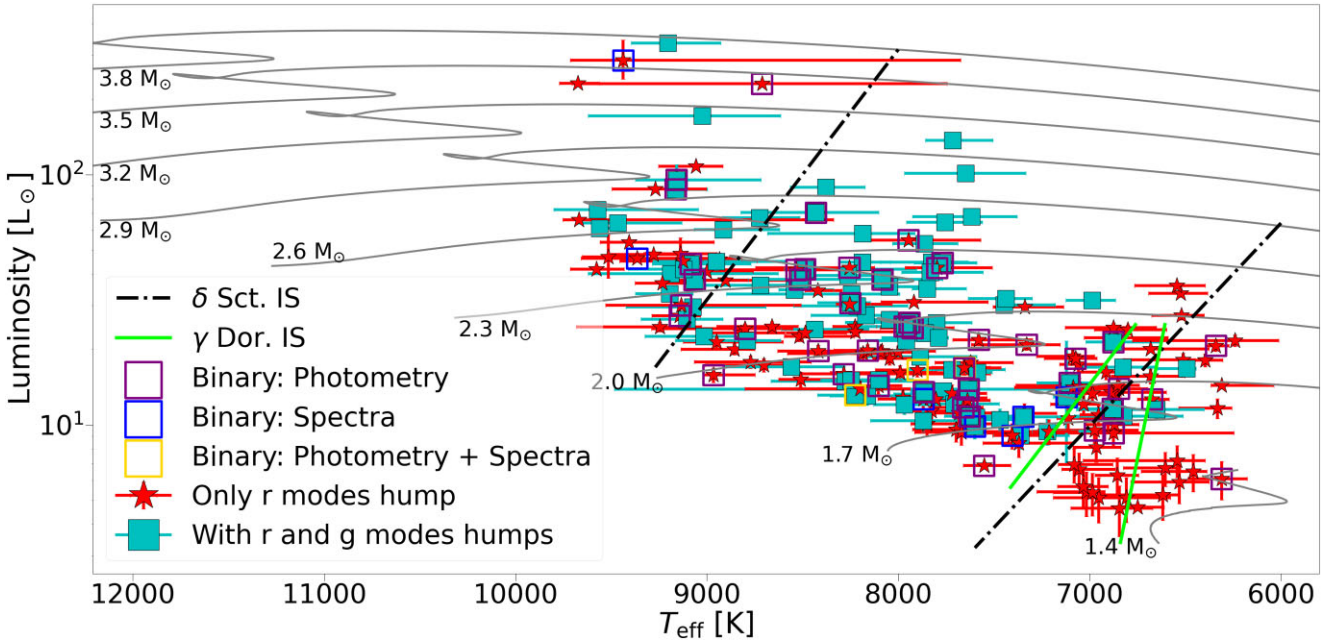

Figure 12. HR diagram displaying 212 stars from our sample. Cyan square and red star symbols depict star with and without g-mode humps, respectively. Some targets are flagged as possible binaries (Binary: Photometry – binarity evidence in photometric data – see example in Fig. 1; Binary: Spectra – see Table 2). In the background, Warszaw–New Jersey evolutionary tracks ($Z = 0.012$; Asplund et al. 2004) are displayed for guidance only. The observed δ Sct. instability strip from Murphy et al. (2019) and the theoretical γ Dor. instability strip (mixing length parameter, $\alpha = 2$) from Dupret et al. (2005) are also displayed. KIC 5458880 and KIC 5980337 are not shown here as no luminosity values could be found in literature. Both these targets are flagged as binaries.

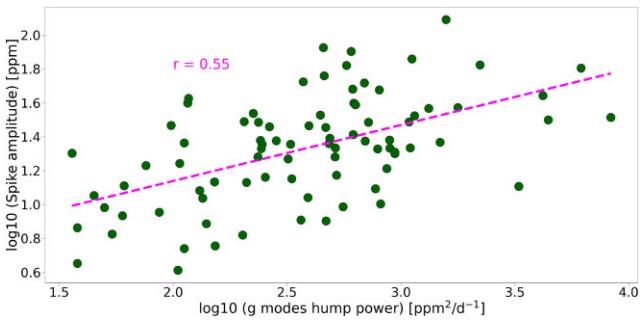

Figure 13. Moderate correlation ($r = 0.55$) between power in the g-mode humps and the amplitudes of the spikes .

Notably, Fig. 14 reveals dips in the frequency range of approximately 0.15–0.25 d^{-1} in models with $M > 1.7$ $M_\odot$, which correspond to the frequencies of g-mode humps. These dips in I_k coincide with the frequencies of the humps due to the fact that a prograde dipole g-mode frequency in the co-rotating frame is equivalent to the frequency difference from the rotation frequency in the observer's frame. Conversely, no such dips appear in less massive models with $M \leq 1.7$ $M_\odot$, which corresponds to the absence of g-mode humps in the cooler side of the instability strip in the HR diagram (see Fig. 12).

To investigate the origin of the differences in g-mode properties among the models displayed in Fig. 14, we show the squared Brunt–Väisälä frequency, N^2, as a function of the interior temperature for each model in Fig. 16. The upper panel shows N^2 for 1.8-, 2.0-, and 2.6-$M_\odot$ models, which exhibit dips in the I_k versus frequency

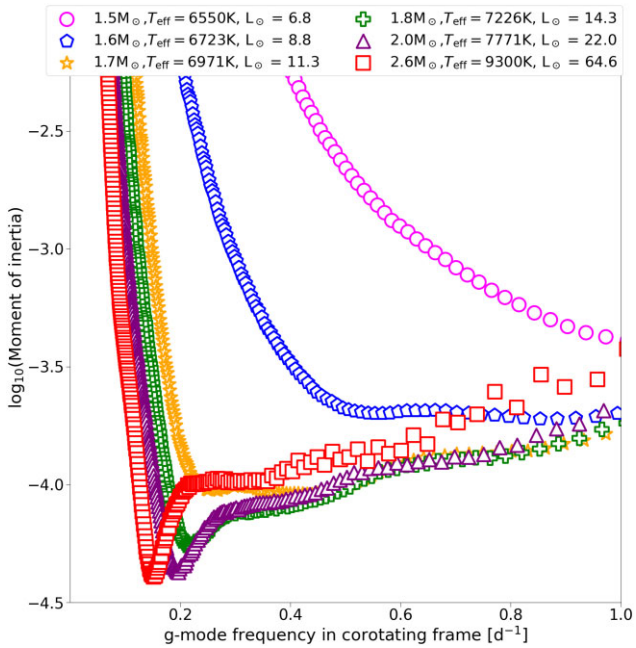

Figure 14. The relationship between the moment of inertia (as defined in equation 5) and the dipole prograde g-mode oscillation frequency in the co-rotating frame for selected stellar models. The models represented here are evolved main-sequence models with central helium abundances of approximately 0.8, which is consistent with the fact that the *hump and spike* stars are also somewhat evolved, as demonstrated in Fig. 12.

Downloaded from https://academic.oup.com/mnras/article/524/3/4196/7210543 by University of Southern Queensland user on 14 December 2023

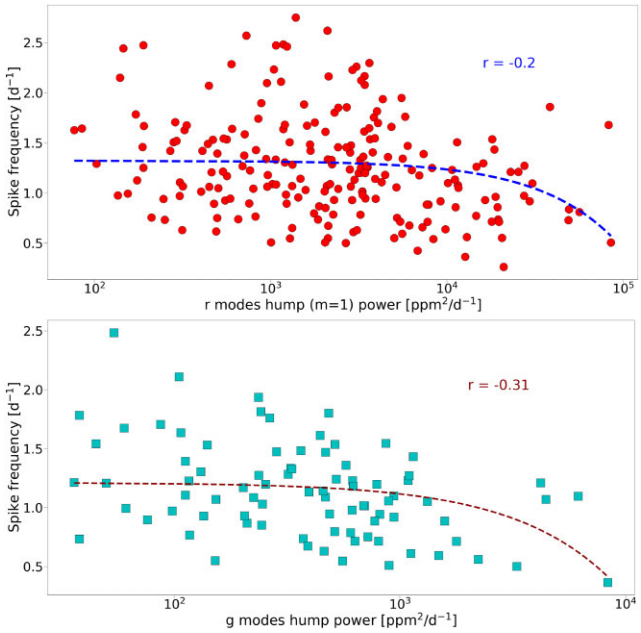

Figure 15. *Upper panel*: Weak anticorrelation ($r = -0.2$) between power in the r-mode humps and the spike frequencies. *Lower panel*: Weak anticorrelation ($r = -0.31$) between power in the g-mode humps and the spike frequencies.

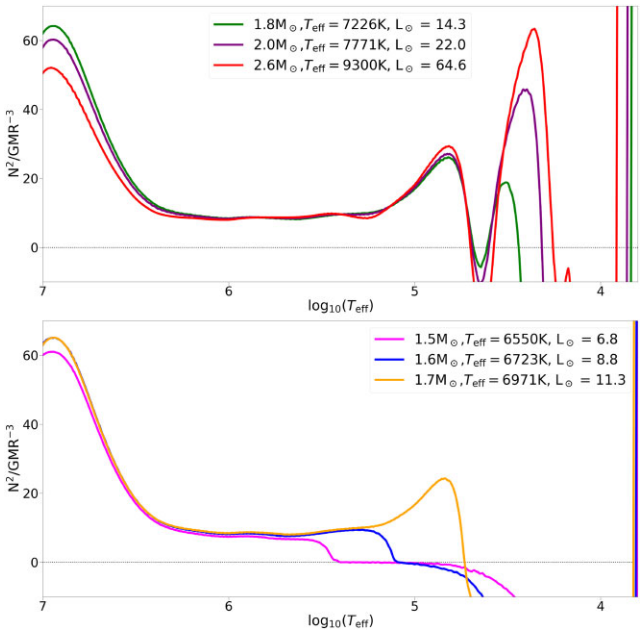

Figure 16. The relationship between the squared normalized Brunt–Väisälä frequency and the logarithmic interior temperature for each model in Fig. 14. The right-hand side of the figure is closest to the surface. *Upper panel*: Data for more massive stars that exhibit a thin radiative zone between the convection zones caused by H/He I and the He II ionization. *Lower panel*: Data for less massive models that lack such a zone.

relation around the frequency range between approximately 0.15 and 0.2 d^{-1}. In contrast, the lower panel displays N^2 for 1.5-, 1.6-, and 1.7-M$_\odot$ models that lack these dips. It is noteworthy that each model in the upper panel has a thin radiative zone between the convection zones associated with H/He I ionization ($4 \lesssim \log_{10} T \lesssim 4.2$) and the

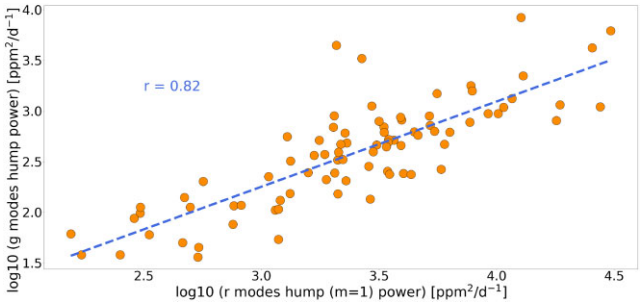

Figure 17. Strong correlation ($r = 0.82$) between the power in the g- and r-mode humps ($m = 1$).

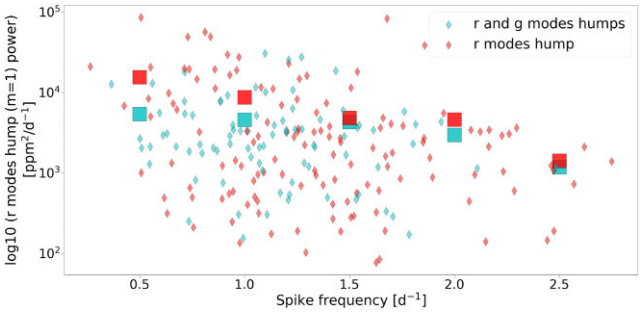

Figure 18. Rotation frequency (spike frequency) as a function of the r-mode hump ($m = 1$) power. Here, we distinguish between stars that exhibit the g-mode hump and those that do not. Small markers in background are the values for each stars. Large markers indicate the average values of r-mode hump ($m = 1$) power for stars with spike frequencies within the following ranges [0.25–0.75], [0.75–1.25], [1.25–1.75], [1.75–2.25], and [2.25–2.75 d^{-1}].

He II ionization at $\log_{10} T \sim 4.6$. Furthermore, the eigenfunction of a g mode at the minimum of the moment of inertia (Fig. 14) has its first node (from the surface) at the bottom boundary of the radiative zone. This observation indicates that the presence of a thin radiative zone between H/He I and He II ionization zones is a necessary condition for the narrow minima in the moment of inertia versus g-mode frequency and hence for the occurrence of g-mode humps. In other words, the absence of the thin radiative zone could explain the lack of g-mode humps in stars located in the cooler side of the δ Sct instability strip (Fig. 12). We note, however, that this conclusion is based on theoretical models, which contain a simplified picture of the physics in the outer stellar envelope. In reality, convection and overshooting are complex phenomena that cannot be fully described in 1D models.

Fig. 13 shows a moderate correlation between the g-mode hump and the amplitude of the spike, suggesting that these are also mechanically excited, by stellar spots or OsC modes. Furthermore, the strong correlation between the r-mode ($m = 1$) and the g-mode humps (Fig. 17) clearly indicates a common mechanism generating the two types of modes.

The weak correlation between the rotation frequency (spike frequency) and the r- and the g-mode humps (upper panel and lower panel, respectively, of Fig. 15) suggests that the rotation rate does not play an essential role in the excitation of these modes. Furthermore, stars that possess the g-mode humps and those that do not are not distinct concerning their rotation rates (see Fig. 18). However, given the low amplitude of the g-mode hump signal, it cannot be excluded that these features may be present in all stars, but buried in the noise.

Downloaded from https://academic.oup.com/mnras/article/524/3/4196/7210543 by University of Southern Queensland user on 14 December 2023

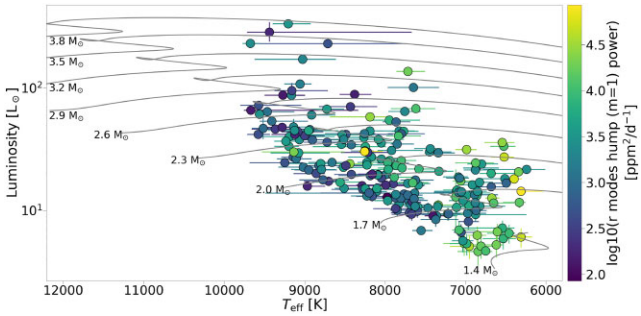

Figure 19. HR diagram with the symbol colour indicating the power in r-mode $m = 1$ humps. In the background, Warszaw–New Jersey evolutionary tracks ($Z = 0.012$; Asplund et al. 2004) are displayed for guidance only. KIC 5458880 and KIC 5980337 are not shown here as no luminosity values could be found in literature. Both these targets are flagged as binaries.

Similar to fig. 17 in Henriksen et al. (2023), where the spike amplitude correlates with the stellar mass, Fig. 19 shows a similar but less obvious trend, of the r-mode $m = 1$ power decreasing with stellar mass. This is not surprising given the correlation displayed in Fig. 11 (upper panel). However, we note that possible companions could contaminate the $T_{\rm eff}$ and luminosity values. It could be that the trend seen in Fig. 19 may become stronger, if more precise and reliable stellar parameters would be determined in the future. Furthermore, a more in-depth focus on the binarity occurrence in *hump and spike* stars would be a valuable endeavour, but more spectroscopic data are required. Given the faintness of the targets, a significant amount of data is required. We note that some stars may have been flagged as binaries in literature; however, their orbital periods turned out to be the spike frequencies, which clearly suggests erroneous identification.

4 CONCLUSIONS

This work is a continuation of the ensemble analysis from Henriksen et al. (2023), where a detailed investigation of the *spike* in *hump and spike* stars was conducted. Here, we concentrate on the *hump* signal and use both *Kepler* photometry and ground-based spectroscopy to characterize 214 stars. We measure the power in r-mode humps and find that a significant number of stars display an additional hump at slightly higher frequencies than the spike, for which we also determine the power. We use spectroscopic data to derive RV measurements and investigate possible binarity. Out of the 22 stars, 11 are consistent with RV shifts due to a companion. Furthermore, we determine $v \sin i$ values for 28 stars and find literature values for additional 61 stars. Together with the rotational velocities derived from the rotational frequencies and stellar radii, we estimate the stellar inclination angle for 89 stars. Based on our results, we conclude the following:

(i) We find a strong correlation between the r- and the g-mode humps and spike amplitudes, suggesting that either stellar spots or OsC modes could indeed induce both types of oscillations mechanically (Figs 11 and 13).

(ii) Rotation does not seem to play an important role, as the spike frequency (due to rotational modulation in the core or at the surface) only weakly correlates the power in either the r- and g-mode humps (Fig. 15). This is consistent with Henriksen et al. (2023), who report no correlation between the spike amplitudes and frequencies.

(iii) The larger the power in the r-mode hump ($m = 1$), the more likely it is for higher azimuthal r modes to be excited and/or visible (upper panel Fig. 11).

(iv) Stars cooler than the observed red δ Scuti instability strip show no g-mode humps, suggesting that the presence of a thin radiative zone between H/He I and He II ionization zones is a necessary condition for the occurrence of g-mode humps (Fig. 12).

We assess that at this stage, neither the stellar magnetic spots nor OsC modes can be excluded as the mechanism for the spike mechanically inducing the r- and g-mode humps. We conclude that detailed modelling of selected stars needs to be conducted; however, the period spacings of high-order r modes cannot be retrieved for these stars. We show that r modes with higher amplitudes would have to be observed for almost a century in order to be resolved, which is unfeasible. To distinguish between the stellar spots or OsC scenarios, we recommend spectro-polarimetric observations of bright *hump and spike* stars that could be identified in the continuous viewing zone of the *TESS* mission. Another open question that should be addressed in future work is, 'why not all A and F stars that show rotational modulation are *hump and spike* stars?' Comparing these two groups of stars may shed more light on this phenomenon.

ACKNOWLEDGEMENTS

Based on observations made with the Nordic Optical Telescope, owned in collaboration by the University of Turku and Aarhus University, and operated jointly by Aarhus University, the University of Turku, and the University of Oslo, representing Denmark, Finland, and Norway, the University of Iceland and Stockholm University at the Observatorio del Roque de los Muchachos, La Palma, Spain, of the Instituto de Astrofisica de Canarias under programs 64-013 and 65-854.

Based on observations made with the Mercator Telescope, operated on the island of La Palma by the Flemish Community, at the Spanish Observatorio del Roque de los Muchachos of the Instituto de Astrofísica de Canarias.

Based on observations obtained with the HERMES spectrograph, which is supported by the Research Foundation – Flanders (FWO), Belgium, the Research Council of KU Leuven, Belgium, the Fonds National de la Recherche Scientifique (F.R.S.-FNRS), Belgium, the Royal Observatory of Belgium, the Observatoire de Genève, Switzerland, and the Thüringer Landessternwarte Tautenburg, Germany.

Based on observations made with the Hertzsprung SONG telescope operated on the Spanish Observatorio del Teide on the island of Tenerife by the Aarhus and Copenhagen Universities and by the Instituto de Astrofísica de Canarias.

This work was supported by a research grant (00028173) from VILLUM FONDEN. Funding for the Stellar Astrophysics Centre is provided by the Danish National Research Foundation (grant agreement no. DNRF106).

This research was supported in part by the National Science Foundation under grant no. NSF PHY-1748958.

DMB gratefully acknowledges funding from the Research Foundation Flanders (FWO) by means of a senior postdoctoral fellowship (grant agreement no. 1286521N).

TVR gratefully acknowledges support from the Research Foundation Flanders (grant no. 12ZB620N) and from the KU Leuven Research Council (grant C16/18/005: PARADISE).

Downloaded from https://academic.oup.com/mnras/article/524/3/4196/7210543 by University of Southern Queensland user on 14 December 2023

DATA AVAILABILITY

The data underlying this article are available in the article and in its online supplementary material. Kepler data can be downloaded from kasoc,phys.au.dk or mast.stsci.edu. Spectroscopic data can be requested via the relevant telescopes websites (FIES - https://www.not.iac.es/archive/, HERMES - https://www.mercator.iac.es/contact/ and SONG - https://soda.phys.au.dk/).

REFERENCES

Abt H. A., 2009, AJ, 138, 28
Andersson N., 1998, ApJ, 502, 708
Asplund M., Grevesse N., Sauval A. J., Allende Prieto C., Kiselman D., 2004, A&A, 417, 751
Balona L. A., 2013, MNRAS, 431, 2240
Balona L. A., 2014, MNRAS, 441, 3543
Balona L. A., 2017, MNRAS, 467, 1830
Balona L. A., Catanzaro G., Abedigamba O. P., Ripepi V., Smalley B., 2015, MNRAS, 448, 1378
Berger T. A., Huber D., van Saders J. L., Gaidos E., Tayar J., Kraus A. L., 2020, AJ, 159, 280
Bertaux J. L., Lallement R., Ferron S., Boonne C., Bodichon R., 2014, A&A, 564, A46
Blanco-Cuaresma S., 2019, MNRAS, 486, 2075
Blanco-Cuaresma S., Soubiran C., Heiter U., Jofré P., 2014, A&A, 569, A111
Boyajian T. S. et al., 2016, MNRAS, 457, 3988
Brown T. M., Latham D. W., Everett M. E., Esquerdo G. A., 2011, AJ, 142, 112
Cantiello M., Braithwaite J., 2019, ApJ, 883, 106
Castelli F., Kurucz R. L., 2003, in Piskunov N., Weiss W. W., Gray D. F.,eds, IAU Symposium, Modelling of Stellar Atmospheres Vol 210. p. A20, preprint(astro-ph/0405087)
Catanzaro G., Frasca A., Molenda-Żakowicz J., Marilli E., 2010, A&A, 517, A3
Dupret M. A., Grigahcène A., Garrido R., Gabriel M., Scuflaire R., 2005, A&A, 435, 927
Eggleton P. P., Tokovinin A. A., 2008, MNRAS, 389, 869
Frasca A. et al., 2016, A&A, 594, A39
Fredslund Andersen M., Handberg R., Weiss E., Frandsen S., Simón-Díaz S., Grundahl F., Pallé P., 2019, PASP, 131, 045003
Gaia Collaboration, 2018, A&A, 616, A1
Gray D. F., 2005, The Observation and Analysis of Stellar Photospheres, 3rd edn. Cambridge Univ. Press, Cambridge
Gray R. O., Corbally C. J., 1994, AJ, 107, 742
Grevesse N., Sauval A. J., 1998, Space Sci. Rev., 85, 161
Henriksen A. I. et al., 2023, MNRAS, 520, 216
Jeffery C. S., 2020, MNRAS, 496, 718
Kahraman Aliçavuş F., Poretti E., Catanzaro G., Smalley B., Niemczura E., Rainer M., Handler G., 2020, MNRAS, 493, 4518
Koch D. G. et al., 2010, ApJ, 713, L79
Lanza A. F., Gizon L., Zaqarashvili T. V., Liang Z. C., Rodenbeck K., 2019, A&A, 623, A50
Lee U., 2021, MNRAS, 505, 1495
Lee U., Saio H., 1997, ApJ, 491, 839
Lee U., Saio H., 2020, MNRAS, 497, 4117
Lehmann H. et al., 2011, A&A, 526, A124
Li G., Van Reeth T., Bedding T. R., Murphy S. J., Antoci V., 2019, MNRAS, 487, 782
Lightkurve Collaboration, 2018, Astrophysics Source Code Library, record ascl:1812.013
Löptien B., Gizon L., Birch A. C., Schou J., Proxauf B., Duvall T. L., Bogart R. S., Christensen U. R., 2018, Nat. Astron., 2, 568
Luck R. E., 2014, AJ, 147, 137
Molenda-Żakowicz J., Brogaard K., Niemczura E., Bergemann M., Frasca A., Arentoft T., Grundahl F., 2014, MNRAS, 445, 2446
Murphy S. J., Hey D., Van Reeth T., Bedding T. R., 2019, MNRAS, 485, 2380
Niemczura E. et al., 2015, MNRAS, 450, 2764
Papaloizou J., Pringle J. E., 1978, MNRAS, 182, 423
Patience J., Ghez A. M., Reid I. N., Matthews K., 2002, AJ, 123, 1570
Paxton B., Bildsten L., Dotter A., Herwig F., Lesaffre P., Timmes F., 2011, ApJS, 192, 3
Paxton B. et al., 2013, ApJS, 208, 4
Paxton B. et al., 2015, ApJS, 220, 15
Provost J., Berthomieu G., Rocca A., 1981, A&A, 94, 126
Raskin G. et al., 2011, A&A, 526, A69
Ricker G. R. et al., 2015, J. Astron. Telesc. Instrum. Syst., 1, 014003
Rossby C.-G., 1939, J. Mar. Res., 2, 38
Royer F., Gerbaldi M., Faraggiana R., Gómez A. E., 2002a, A&A, 381, 105
Royer F., Grenier S., Baylac M. O., Gómez A. E., Zorec J., 2002b, A&A, 393, 897
Saio H., 1982, ApJ, 256, 717
Saio H., 2018, in Ballot J., Vauclair S., Vauclair G., eds, Proceedings of the PHysics of Oscillating STars (PHOST) Conference, R-mode Oscillations Ubiquitous in Stars, Vol 1. France,p.41
Saio H., Kurtz D. W., 2022, MNRAS, 511, 560
Saio H., Kurtz D. W., Murphy S. J., Antoci V. L., Lee U., 2018a, MNRAS, 474, 2774
Saio H., Bedding T. R., Kurtz D. W., Murphy S. J., Antoci V., Shibahashi H., Li G., Takata M., 2018b, MNRAS, 477, 2183
Saio H., Takata M., Lee U., Li G., Van Reeth T., 2021, MNRAS, 502, 5856
Santos A. R. G., Breton S. N., Mathur S., García R. A., 2021, ApJS, 255, 17
Sikora J., Wade G. A., Rowe J., 2020, MNRAS, 498, 2456
Simón-Díaz S., Herrero A., Esteban C., Najarro F., 2006, A&A, 448, 351
Smith M. A., Gray D. F., 1976, PASP, 88, 809
Takata M., Ouazzani R. M., Saio H., Christophe S., Ballot J., Antoci V., Salmon S. J. A. J., 2020, A&A, 644, A138
Telting J. H. et al., 2014, Astron. Nachr., 335, 41
Tkachenko A., Lehmann H., Smalley B., Uytterhoeven K., 2013, MNRAS, 431, 3685
Trust O., Jurua E., De Cat P., Joshi S., 2020, MNRAS, 492, 3143
Trust O., Jurua E., De Cat P., Joshi S., Lampens P., 2021, MNRAS, 504, 5528
Twicken J. D., Chandrasekaran H., Jenkins J. M., Gunter J. P., Girouard F., Klaus T. C., 2010, in Radziwill N. M., Bridger A., eds, Proc. SPIE Conf. Ser. Vol. 7740, Software and Cyberinfrastructure for Astronomy. SPIE, Bellingham, p. 77401U
Van Reeth T., Tkachenko A., Aerts C., 2016, A&A, 593, A120
Virtanen P. et al., 2020, Nat. Methods, 17, 261
Zucker S., 2003, MNRAS, 342, 1291

SUPPORTING INFORMATION

Supplementary data are available at *MNRAS* online.

spectra_meta_data.txt
table_second_harmonic.csv
table_spike_hump_stars_param.csv
table_vsini_inclination.csv

Please note: Oxford University Press is not responsible for the content or functionality of any supporting materials supplied by the authors. Any queries (other than missing material) should be directed to the corresponding author for the article.

Downloaded from https://academic.oup.com/mnras/article/524/3/4196/7210543 by University of Southern Queensland user on 14 December 2023

APPENDIX A: SOME EXTRA MATERIAL

Table A1. Spectroscopic observations analysed in this work – metadata. KIC – *Kepler* input catalogue identification number; Instrument – spectrograph with which the spectrum was acquired; Mid-timestamp = Mid-point of observation; and exposure time in seconds. Only the first 10 rows are displayed here. The full table is available online; here, the first 10 rows are shown for guidance on content and style. The full version contains 75 lines.

KIC	Instrument	Filename	Mid-timestamp	Exposure time (s)
3634487	FIES	FIFf190083.fits	2022-06-20T00:36:29	1200
3634487	FIES	FIFe260039.fits	2022-05-27T00:38:37	1200
3848948	FIES	FIFf190107.fits	2022-06-20T03:55:55	1100
3848948	FIES	FIFe250037.fits	2022-05-26T02:10:21	1100
4066110	FIES	FIEj160096.fits	2021-10-16T21:29:23	1500
4066110	FIES	FIEj160097.fits	2021-10-16T21:55:10	1500
4066110	FIES	FIEj160098.fits	2021-10-16T22:20:57	1500
4572373	HERMES	00413721_HRF_OBJ.fits	2012-07-14T01:55:49	2400
4572373	HERMES	00419068_HRF_OBJ.fits	2012-09-05T00:43:08	1800
4572373	HERMES	00419069_HRF_OBJ.fits	2012-09-05T01:13:58	1800

Table A2. $v \sin i$ values taken from literature and measured in this work, and the estimated inclination values. The full table is available online; here, the first 10 rows are shown for guidance on content and style. The full version contains 87 lines.

KIC	$v \sin i$ (km s^{-1})	$\sigma_{v \sin i}$ (km s^{-1})	Ref. $v \sin i$	i (deg)	σ_i (deg)
3459226	73	5	1	61	8
3634487	175	14	0	62	8
3766112	332	33	2	75	7
3848948	98	12	0	53	9
3868032	181	9	3	59	5
4059089	280	72	2	56	15
4066110	138	19	0	66	11
4481029	136	88	2	32	28
4488313	208	54	2	58	15
4567097	83	5	1	24	2

Notes. Ref. ($v \sin i$ source): (0) This work; (1) Trust et al. (2021); (2) Frasca et al. (2016); (3) Kahraman Aliçavuş et al. (2020); (4) Niemczura et al. (2015); (5) Lehmann et al. (2011); (6) Catanzaro et al. (2010); (7) Sikora, Wade & Rowe (2020); (8) Tkachenko et al. (2013); (9) Boyajian et al. (2016); and (10) Molenda-Żakowicz et al. (2014). i, σ_i: Stellar inclination and its uncertainty.

Table A3. Extracted spike and hump parameters, and stellar parameters. R, R_p, R_m: Radius value and upper and lower uncertainties; R ref. (radius source): b = Berger et al. (2020), g2 = *Gaia* DR2, g3 = *Gaia* DR3, and k = *Kepler* Input Catalogue v10 (Brown et al. 2011); f_{rot}, $\sigma_{f_{rot}}$: Spike frequency and associated standard deviation; A_{rot}: Spike amplitude; v_{rot}, v_{rot_p}, v_{rot_m}: Rotational velocity and associated uncertainties; T_{eff}, T_{eff_p}, T_{eff_m}: Effective temperature and upper and lower uncertainties – from *Gaia* DR2, except for KIC 8462852 (taken from Boyajian et al. 2016); L, L_p, L_m: Luminosity and upper and lower uncertainties; L ref. (luminosity source): b = Berger et al. (2020), b16 = Boyajian et al. (2016), g = *Gaia* DR2, and m = Murphy et al. (2019); Power_{hump}: Power in the r-mode hump; and f_{hump_l}, f_{hump_r}: Lower and higher frequency limits of the hump. The full table is available online; here, the first 10 rows are shown for guidance on content and style. The full version contains 215 lines. Note that there are two lines for KIC 5980337 as there are two *hump and spike* features that could originate from a binary system. No luminosity values are given for KIC 5458880 and KIC 5980337.

KIC	R ($R_\odot$)	R_p ($R_\odot$)	R_m ($R_\odot$)	R ref.	f_{rot} (d^{-1})	$\sigma_{f_{rot}}$ (d^{-1})	A_{rot} (ppm)	v_{rot} (km s^{-1})	v_{rot_p} (km s^{-1})	v_{rot_m} (km s^{-1})	T_{eff} (K)	T_{eff_p} (K)	T_{eff_m} (K)	L ($L_\odot$)	L_p ($L_\odot$)	L_m ($L_\odot$)	L ref.	Power_{hump} (ppm^2 d)	f_{hump_l} (d^{-1})	f_{hump_r} (d^{-1})
1722916	1.5	0.03	0.03	g3	0.553	0.0013	44	42	1	1	7017	260	98	5.4	1.09	1.09	m	20 556	0.455	0.530
1873552	1.6	0.04	0.04	g3	1.236	0.0016	5	100	3	3	7826	121	86	11.4	1.05	1.06	m	2818	1.024	1.221
2157489	1.9	0.04	0.04	g3	0.737	0.0014	53	71	1	1	7361	140	254	9.1	1.05	1.05	m	1859	0.644	0.728
2158190	2.8	0.11	0.09	b	1.016	0.0006	24	144	6	5	8048	42	219	35.6	1.05	1.05	m	3317	0.934	1.008
3002336	2.4	0.05	0.06	g3	1.202	0.0004	76	146	3	4	7115	272	217	14.4	1.06	1.07	m	3254	1.056	1.190
3222104	2.1	0.07	0.07	g3	1.270	0.0004	23	135	4	4	8821	231	228	23.3	1.08	1.08	m	694	1.095	1.263
3238627	2.8	0.08	0.08	g3	1.537	0.0024	23	218	6	6	7059	98	140	17.4	1.10	1.10	m	18 076	1.444	1.530
3240406	1.9	0.04	0.04	g3	1.071	0.0013	6	103	2	2	7865	161	201	13.3	1.06	1.06	m	1324	0.972	1.066
3337124	1.8	0.14	0.03	g2	1.108	0.0004	23	101	8	2	7835	61	298	12.8	1.05	1.05	m	4268	0.962	1.101
3440710	1.6	0.04	0.04	g3	1.250	0.0021	33	101	3	3	6531	256	154	5.9	1.06	1.06	m	8248	1.075	1.242

Downloaded from https://academic.oup.com/mnras/article/524/3/4196/7210543 by University of Southern Queensland user on 14 December 2023

Table A4. Wavelength limits of the sections into which the HERMES spectra were split.

Section	Wavelength limits	
	Blue (Å)	Red (Å)
1	4000	4225
2	4225	4450
3	4450	4550
4	4550	4650
5	4650	4750
6	4750	5034
7	5087	5200
8	5200	5414
9	5462	5683
10	5754	5870
11	6000	6275
12	6361	6432
13	6600	6800

Table A5. Spectral lines used for $v \sin i$ determination. The resulting $v \sin i$ values are listed next to the corresponding spectral lines (denoted by the species, ionization state, and wavelength) for each star (identified with KIC ID). In some cases, an additional identifier for the used line is the échelle order, as some lines can be found in two adjacent orders that overlap (e.g. order 27 and order 28 = o27, o28). The final $v \sin i$ values are listed in Table 4 as the average values obtained from all spectral lines.

KIC	Spectral line (Å)	$v \sin i$ (km s^{-1})	KIC	Spectral line (Å)	$v \sin i$ (km s^{-1})	KIC	Spectral line (Å)	$v \sin i$ (km s^{-1})
3634487	Fe II 4508.29 (o27)	177	5938266	Fe I 6065.48	112	7939835	Ti II 4501.27	25
	Fe II 4508.29 (o28)	177		Fe I 6078.49	109		Fe II 4508.29 (o27)	23
	Ti II 4571.97	154		Fe I 6393.61	114		Fe II 4508.29 (o28)	21
	Ca I 6439.07	192		Ca I 6439.07	76		Ti II 4571.97	23
3848948	Fe II 4508.29 (o27)	97	5980337	Fe I 6055.99	77		Fe II 4923.93	17
	Fe II 4508.29 (o28)	112		Fe I 6065.48	111		Fe I 5862.35	18
	Ti II 4571.97	80		Ca I 6122.22	67		Fe I 5934.65	38
	Ca I 6439.07	104		Ca I 6439.07	91		Fe I 6020.17	26
4066110	Fe I 6065.48	140	6039039	Fe I 5862.35	75		Fe I 6024.05	19
	Fe I 6078.49	161		Fe I 6055.99	81		Fe I 6055.99	34
	Ca I 6439.07	114		Fe I 6065.48	85		Fe I 6065.48	24
4661914	Fe I 5633.98	84		Fe I 6078.49	79		Ca I 6122.22	18
	Fe I 5905.69	94		Ca I 6122.22	66		Fe I 6393.61	27
	Fe I 6065.48	62	6192566	Fe II 4508.29	48		Ca I 6439.07	17
	Fe I 6078.49	100		Ti II 4571.97	47	7959579	Fe I 6065.48	120
4856799	Fe I 4404.76	186		Fe I 6055.99	56		Fe I 6078.49	120
	Fe II 4508.29 (o27)	177		Fe I 6065.48	65		Fe I 6393.61	109
	Fe II 4508.29 (o28)	182		Ca I 6122.22	32		Ca I 6439.07	120
	Ti II 4571.97	173		Fe I 6393.61	59	8037519	Si II 6371.35	177
	Fe II 4923.93	147	6610433	Fe II 4508.29 (o27)	110		Mn II 4481.13/33	196
5024410	Fe I 4454.39	7		Fe II 4508.29 (o28)	126	8783760	Ti II 4779.99	105
	Fe I 4508.29	8		Fe I 5633.98	119		Fe I 6065.48	148
	Ti I 4518.02	7		Ca I 6439.07	117		Fe I 6078.49	144
	Ti I 4548.76	5	6974705	Mn II 4481.13/33	246		Ca I 6122.22	124
	Ti II 4563.76	7	7116117	Fe I 5633.98	72		Ca I 6439.07	116
	Fe II 4576.34	6		Fe I 5905.69	80	8846809	Fe II 4508.29 (o27)	162
	Ti II 4583.41	8		Fe I 6065.48	54		Ti II 4571.97	161
	Cr II 4588.2	7		Fe I 6078.49	76		Fe I 6065.48	140
	Fe I 4602.94	11	7131587	Fe II 4508.29 (o27)	40	9163520	Fe II 4508.29	37
	Cr I 4652.15	6		Fe II 4508.29 (o28)	44		Fe I 5576.09	42
	Mn I 4739.09	10		Fe I 5862.35	52		Fe I 6055.99	47
	Fe I 4741.53	6		Fe II 5987.07	55		Fe I 6065.48	40
	Fe II 4923.93	12		Fe II 6020.17	34		Fe I 6078.49	35
	Fe I 5090.77	9		Fe I 6024.05	48		Fe I 6393.61	44
	Fe I 5141.74	5		Fe I 6027.05	58	9273647	Fe I 6065.48	121
	Fe I 5151.91	6		Fe I 6055.99	44		Fe I 6078.49	123
	Ti I 5210.39	6		Fe I 6065.48	50		Fe I 6393.61	112

Downloaded from https://academic.oup.com/mnras/article/524/3/4196/7210543 by University of Southern Queensland user on 14 December 2023

Table A5 – *continued*

KIC	Spectral line (Å)	$v \sin i$ (km s^{-1})	KIC	Spectral line (Å)	$v \sin i$ (km s^{-1})	KIC	Spectral line (Å)	$v \sin i$ (km s^{-1})
	Fe I 5364.86	10		Fe I 6078.49	64		Ca I 6439.07	108
	Fe I 5398.28	12		Si II 6371.36 (o64)	47	9519698	Fe I 4404.76	182
	Fe I 5862.35	6		Si II 6371.36 (o65)	54		Fe II 4508.29 (o27)	177
	Fe I 6024.05	4		Fe I 6430.86	41		Fe II 4508.29 (o28)	177
	Fe I 6065.48	6		Ca I 6439.07	39		Ti II 4571.97	177
	Ca I 6122.22	7		Ca I 6471.67	60		Fe II 4923.93	164
	Fe I 6252.57	5	7842339	Fe I 4404.76	93	10068389	Ti II 4501.27	124
	Fe I 6393.61	6		Fe II 4508.29	101		Fe II 4508.29 (o27)	133
5456027	Fe II 4508.29 (o27)	158		Ca I 6439.07	119		Fe II 4508.29 (o28)	127
	Fe II 4508.29 (o28)	156					Ti II 4571.97	127
	Ti II 4571.97	157					Ca I 6439.07	150
	Ca I 6439.07	171				10810140	Ti II 4501.27	136
5566579	Fe II 4515.34	169					Fe II 4508.29 (o27)	133
	Ti II 4571.97	128					Fe II 4508.29 (o28)	129
	Fe II 4923.93	125					Ti II 4571.97	128
5903499	Mn II 4481.13/33	254					Ca I 6439.07	122

Table A6. Information about the second harmonic of the spike and $m = 2$ r-mode hump. f, σ_f: Frequency of second harmonic of the spike and associated standard deviation; $A_{\rm rot}$: Amplitude of second harmonic of the spike; Power$_{\rm hump}$: Power in the $m = 2$ r-mode hump; and $f_{\rm hump_l}$, $f_{\rm hump_r}$: Lower and higher frequency limits of the $m = 2$ r-mode hump. Only the first 10 rows are displayed here. The full table is available online; here, the first 10 rows are shown for guidance on content and style. The full version contains 112 lines.

KIC	f (d^{-1})	σ_f (d^{-1})	A (ppm)	Power$_{\rm hump}$ (ppm^2 d)	$f_{\rm hump_l}$ (d^{-1})	$f_{\rm hump_r}$ (d^{-1})
1722916	1.105	0.0014	10.0	686	0.958	1.016
2157489	1.474	0.0004	7.8	194	1.326	1.467
2158190	2.032	0.0006	6.3	148	1.908	2.017
3238627	3.077	0.0005	18.5	2152	2.976	3.060
3240406	2.141	0.0008	4.4	68	1.999	2.096
3337124	2.216	0.0004	3.4	183	1.911	2.200
3440710	2.501	0.0021	19.3	1128	2.319	2.487
3766112	4.463	0.0007	4.8	70	4.355	4.459
3848948	2.574	0.0006	2.0	45	2.403	2.568
3868032	3.358	0.0019	6.7	24 636	0.754	0.819

This paper has been typeset from a TEX/LATEX file prepared by the author.

Downloaded from https://academic.oup.com/mnras/article/524/3/4196/7210543 by University of Southern Queensland user on 14 December 2023

© 2023 The Author(s)
Published by Oxford University Press on behalf of Royal Astronomical Society